Available online at www.sciencedirect.com
ScienceDirect
Journal of Solid State Chemistry 179 (2006) 3860–3869
JOURNAL OF SOLID STATE CHEMISTRY
www.elsevier.com/locate/jssc

Unit-cell intergrowth of pyrochlore and hexagonal tungsten bronze structures in secondary tungsten minerals

Ian E. Grey[a,*], William D. Birch[b], Catherine Bougerol[c], Stuart J. Mills[a,b]

[a]*CSIRO Minerals, Box 312, Clayton South, Vic. 3169, Australia*
[b]*Geosciences Department, Museum Victoria, GPO Box 666, Melbourne, Vic. 3001, Australia*
[c]*Equipe CEA-CNRS NPSC SP2M/DRFMC/CEA, 17 rue des Martyrs, 38054 Grenoble, France*

Received 11 May 2006; received in revised form 15 August 2006; accepted 16 August 2006
Available online 1 September 2006

Abstract

Structural relations between secondary tungsten minerals with general composition $A_x[(W,Fe)(O,OH)_3]_{.y}H_2O$ are described. Phyllotungstite (A = predominantly Ca) is hexagonal, $a = 7.31(3)$ Å, $c = 19.55(1)$ Å, space group $P6_3/mmc$. Pittongite, a new secondary tungsten mineral from a wolframite deposit near Pittong in Victoria, southeastern Australia (A = predominantly Na) is hexagonal, $a = 7.286(1)$ Å, $c = 50.49(1)$ Å, space group $P\text{-}6m2$. The structures of both minerals can be described as unit-cell scale intergrowths of $(111)_{py}$ pyrochlore slabs with pairs of hexagonal tungsten bronze (HTB) layers. In phyllotungstite, the $(111)_{py}$ blocks have the same thickness, 6 Å, whereas pittongite contains pyrochlore blocks of two different thicknesses, 6 and 12 Å. The structures can alternatively be described in terms of chemical twinning of the pyrochlore structure on $(111)_{py}$ oxygen planes. At the chemical twin planes, pairs of HTB layers are corner connected as in hexagonal WO_3.

Keywords: Chemical twinning of pyrochlore; Structures of secondary tungsten minerals; Unit-cell intergrowth structures; Pittongite; Phyllotungstite

1. Introduction

Supergene and hydrothermal alteration of the tungstate minerals ferberite, $FeWO_4$, and scheelite, $CaWO_4$, provides a rich variety of secondary tungsten minerals, including ferritungstite, aluminotungstite, jixianite, elsmoreite, hydrotungstite, tungstite, anthoinite and phyllotungstite [1–4]. The compositions of these secondary minerals conform to the general formula $A_x[(W,Fe,Al)(O,\ OH)_3]_{.y}H_2O$, $x = 0$ to 0.33, $y = 0$ to 2, where $A = H_2O$ and large cations such as Na^+, Ca^{2+}, K^+, Pb^{2+}. The minerals are generally very fine grained and the lack of suitable sized crystals for single-crystal structure analysis has hampered detailed structural analyses in many cases. Exceptions are ferritungstite [2] and elsmoreite [4] having pyrochlore-type $A_2M_2O_7$ structures, and tungstite [5] having layers of ReO_3-type corner-connected octahedra. From the similarity of its diffraction data to that for molybdic acid, hydrotungstite is also considered to have a layer structure with the layers composed of ReO_3-type corner-connected octahedra [6]. The ReO_3-type structure is shown in Fig. 1(a).

Further structural information on hydrated tungstic oxides is available from studies on synthetic materials prepared by hydrothermal methods. $WO_3 \cdot 1/3H_2O$ [7] and $WO_3 \cdot 1/2H_2O$ [8] have structures containing hexagonal tungsten bronze-type (HTB) layers of corner-connected octahedra. The HTB-type layer is shown in Fig. 1(b). A feature of the HTB layer is the presence of hexagonal rings that can be occupied by large A cations. In cubic $WO_3 \cdot 1/2H_2O$, which is isostructural with elsmoreite and ferritungstite, the HTB layers are normal to each of the four $\langle 111 \rangle$ axes, giving a pyrochlore-type W_2O_6 octahedral framework. The A sites are vacant and the H_2O occupies an O site. In $WO_3 \cdot 1/3H_2O$ the HTB layers are stacked along one axis and connected by corner linking of two-thirds of the WO_6 octahedra. Controlled heating of $WO_3 \cdot 1/3H_2O$ gives a hexagonal form of the oxide, h-WO_3, [9] in which HTB layers are stacked along [001] with corner sharing of all octahedra as shown in Fig. 1(c). At higher

*Corresponding author. Fax: +61 3 9562 8919.
E-mail address: ian.grey@csiro.au (I.E. Grey).

0022-4596/$ - see front matter © 2006 Elsevier Inc. All rights reserved.
doi:10.1016/j.jssc.2006.08.030

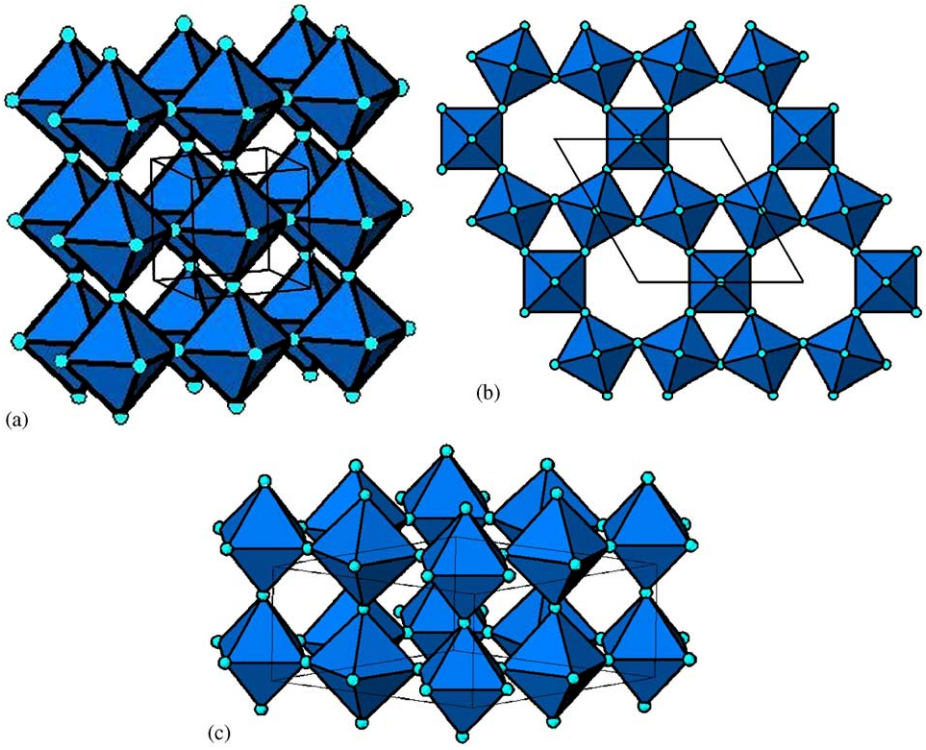

Fig. 1. Polyhedral representations of (a) ReO_3 structure, (b) a layer of hexagonal tungsten bronze type and (c) pair of HTB layers as in h-WO_3.

temperatures, h-WO_3 transforms to monoclinic WO_3 having a 3-D ReO_3-type topology [10]. In summary, the structures of the characterized synthetic and mineral-form hydrated tungstic oxides are all based on either ReO_3-type or HTB-type 2-D and 3-D networks of corner-linked octahedra.

In a recent Mineralogical Society of Victoria excursion to a wolframite deposit near Pittong in Victoria, southeastern Australia, a sample containing yellow encrustations of tiny crystals on etched manganoan ferberite was collected. The crystals are very thin ($\sim$0.3 μm) curved plates as shown in Fig. 2, that are stacked together in aggregates of up to 0.2 mm across or in the form of compact masses. Analysis of the yellow platelets showed that they corresponded to a hydrated tungstic oxide phase containing significant amounts of iron and sodium. A powder X-ray diffraction (PXRD) pattern of the mineral showed similarities with the published pattern for phyllotungstite [11], a hydrated tungstic oxide containing iron and calcium. The mineral has been been accepted as a new mineral with the name pittongite by the IMA Commission on New Minerals and New Mineral Names. Crystal chemical reasoning, supported by results from transmission electron microscopy (TEM) studies, led to the development of a general structural model for pittongite and phyllotungstite. The model is based on unit-cell intergrowth of $(111)_{py}$ slabs of pyrochlore type with layers of HTB-type structures. Pittongite and phyllotungstite represent two different intergrowth sequences, or polytypes. We report here the development of structural models that are consistent with the PXRD and TEM data.

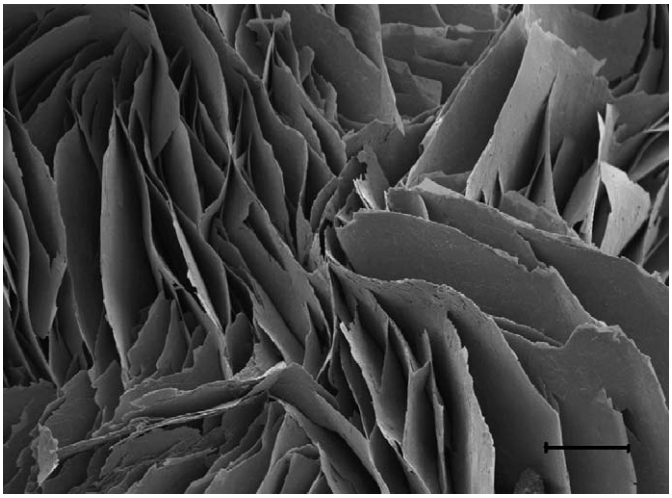

Fig. 2. Scanning electron microscope image of crystals of pittongite. Scale bar = 20 μm.

2. Experimental

Full details of the mode of occurrence, paragenesis, physical and optical properties of pittongite will be reported elsewhere [12]. Elemental analyses of the crystals were conducted using a Cameca SX 50 electron microprobe in wavelength dispersive mode, operated at 15 kV and 20 nA. Standards used were albite (Na), wollastonite (Ca),

hematite (Fe), corundum (Al), tungsten metal and synthetic $KTaO_3$ (K). Water was determined using a Carlo Erba 1106 CHN analyser.

A synchrotron X-ray powder diffraction pattern for pittongite was obtained using the Australian high-resolution powder diffractometer (Big Diff) at the Photon Factory, Tsukuba, Japan. The mineral was finely ground and packed in a 1 mm Lindeman capillary for the data collection. Partial diffraction rings were collected on image plates, located 573 mm from the axially spinning sample. Data were collected at a wavelength of 0.800 Å and calibrated using an Y_2O_3 standard. Rietveld fitting of the synchrotron data was carried out using the Rietveld program SR5 [13].

TEM was conducted using a JEOL 4000EX microscope with a spherical aberration coefficient of 1.06 mm. The microscope was operated at 400 kV. The sample was finely ground with ethanol in an agate mortar and pestle, and the suspension was transferred to a holey carbon grid for the study.

3. Results

The mean analytical results (in wt%) from seven microprobe point analyses and duplicate H_2O analyses on pittongite are 2.97% Na_2O, 0.06% K_2O, 0.39% CaO, 5.66% Fe_2O_3, 0.51% Al_2O_3, 84.15% WO_3 and 4.73% H_2O. These analyses are combined with information on the structure model to establish the unit-cell composition for pittongite in the Discussion section.

The low-angle region of the synchrotron powder diffraction pattern for pittongite is shown in Fig. 3. A feature of the diffraction data is the presence of both sharp and broadened peaks. The pattern was indexed with the aid of precession photographs and selected area electron diffraction (SAED) patterns. Examples of SAED patterns obtained along [001] and [110] zone axes are shown in Figs. 4(a) and (b), respectively. The [001] zone axis SAED pattern displays hexagonal symmetry with $a \sim 7.29$ Å. The determination of c was hampered by the poor quality and ultra-thin nature of the pittongite crystals as shown in Fig. 2. The c-axis is normal to the platelets and SAED patterns displayed streaking and some diffuseness of the reflections along c^* as shown in Fig. 4(b). The positions of the (00l) reflections were consistent with an average c-axis periodicity of ~50.5 Å. The hexagonal cell parameters obtained from the measurements off the SAED patterns were refined using the PXRD data, giving $a = 7.286(1)$ Å, $c = 50.49(1)$ Å.

The published PXRD peak positions and relative intensities for phyllotungstite [11] are also presented in Fig. 3 to illustrate the close relationship between the patterns for the two minerals. Phyllotungstite is reported to have orthorhombic symmetry, with $a = 7.29$ Å, $b = 12.59$ Å, $c = 19.55$ Å. However it was commented in Ref. [11] that suitable single crystals were not available and so the cell parameters were determined from a powder pattern. The value of b is close to $\sqrt{3}a$, suggesting that the

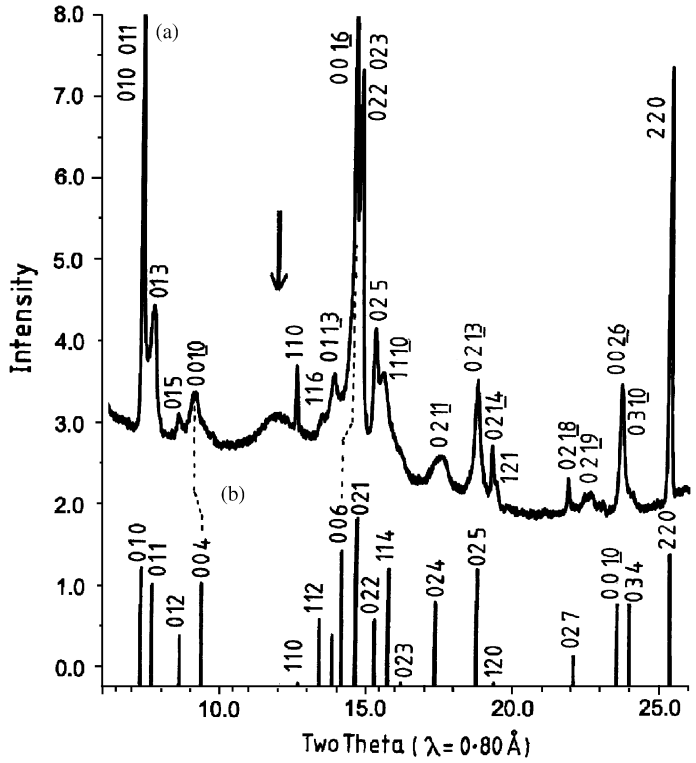

Fig. 3. (a) Part of the synchrotron X-ray powder pattern for pittongite. (b) Peak positions and relative intensities for phyllotungstite, from Ref. [11]. Reflection indices for the hexagonal cell are shown above the peaks. The arrow in (a) identifies a broad peak due to a surface coating of hexagonal WO_3.

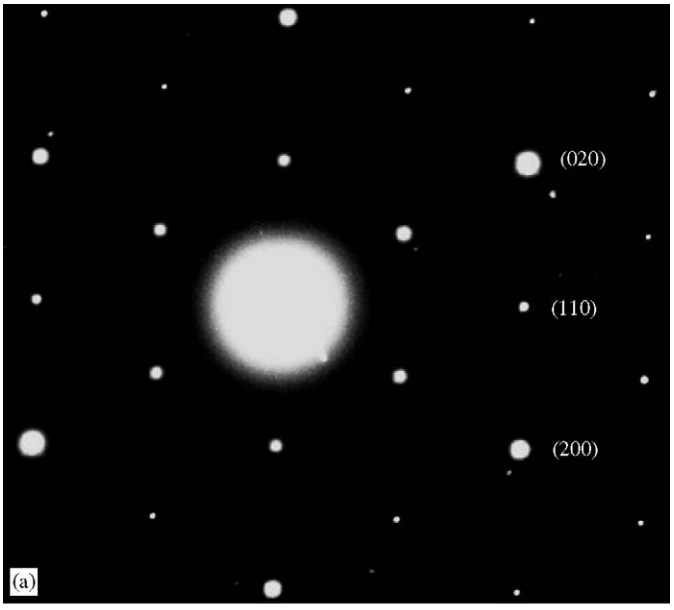

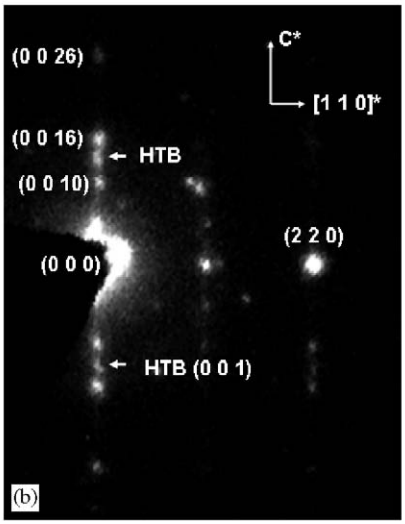

Fig. 4. Selected area electron diffraction patterns for pittongite. (a) [001] zone axis, (b) [110] zone axis.

cell may in fact be hexagonal. We used CELLREF [14] to refine the powder data from [11] using both the reported orthorhombic cell, and a hexagonal cell. We obtained an equally satisfactory fit to the published d spacings using the hexagonal cell with $a = 7.31(3)$ Å, $c = 19.55(1)$ Å. Indices based on this cell are shown for phyllotungstite in Fig. 3. On the basis of the hexagonal cell indexing, the systematic extinctions in the PXRD pattern for phyllotungstite are $(00l)$, $l \neq 2n$ and (hhl), $l \neq 2n$, corresponding to space groups $P6_3/mmc$, $P\text{-}62c$ or $P6_3mc$.

A comparison of the two PXRD patterns shows a close match for the $(hk0)$ reflections, which are the sharp reflections in the pattern for pittongite. Reflections with $l \neq 0$ are generally broadened. The positions for the $(00l)$ reflections for pittongite are displaced from the corresponding reflections for phyllotungstite in a way that is characteristic of structures built from ordered intergrowth of two parent structures [15]. The displacements are in opposite directions for certain pairs of reflections, as illustrated by the dashed lines in Fig. 3 for $[(004), (006)]_{\text{phyllotungstite}}$ and $[(0\,0\,10), (0\,0\,16)]_{\text{pittongite}}$. In intergrowth structures, such displacements are due to changes in the relative widths of the two basic structure types that are intergrown. The PXRD pattern for pittongite contains additional broad reflections such as that marked with an arrow in Fig. 3 that do not occur in the pattern for phyllotungstite. The TEM study revealed that these were impurity peaks due to a very thin film of a surface alteration phase having the h-WO_3 structure.

Direct information on the nature of the intergrowth structure in pittongite was obtained from TEM images. The intergrowth direction is parallel to c, so to obtain relevant images containing the c-axis it was necessary to orient the thin platelets on their edge. This was difficult to accomplish in the TEM and when achieved the images were not well resolved because of the relatively thick projection direction. Nevertheless, structurally interpretable fringe patterns were obtained in a number of [110] and $[1\bar{1}0]$ zone axis images. Fig. 5(a) is typical, showing a platelet edge-on of width ~30 nm, containing a succession of fringes parallel to (001) of two different widths, 9.7 or 6.0 Å.The platelet has a thin rim on each side, only 3 nm wide, of a phase with 3.7 Å fringes parallel to (001). The 3.7 Å fringes in the rim phase, which is most likely a surface alteration product, are clearly defined in Fig. 5(b). In this figure, the 9.7 Å (001) fringes are resolved into pairs of fringes with separation 3.7 and 6 Å. In Fig. 5(c), which is a [110] zone axis image, the (001) 9.7 and 6 Å fringes are resolved along their length into bright spots separated by 6.3 Å.

4. Development of structural models

We used crystal-chemistry reasoning to develop models for pittongite and phyllotungstite. As mentioned in the Introduction, the hydrated tungstic oxides with known structures can all be described as either ReO_3-type or HTB-type derivatives. Unit cells of the ReO_3-type derivatives have near-orthogonal combinations of axes that are multiples of either $a_{ReO_3} \sim 3.8$ Å or $\sqrt{2}a_{ReO_3}$, whereas structures built from HTB-type layers are described by hexagonal or orthohexagonal axes with $a_{HTB} \sim 7.3$ Å. This includes the pyrochlore-type structure, which is usually cubic, $a_{py} \sim 10.3$ Å, but can be described in a hexagonal cell with $a_{hex} = a_{py}/\sqrt{2} = 7.28$ Å, $c_{hex} = \sqrt{3}.a_{py} = 17.8$ Å. A rhombohedrally distorted WO_3 pyrochlore has been reported, with hexagonal cell parameters similar to these values [16]. In rhombohedral pyrochlore, one of the four equivalent $(111)_{py}$ HTB planes becomes the unique $(001)_{hex}$ plane in the hexagonal cell. The 7.3 Å hexagonal cell common to pittongite and to phyllotungstite is consistent with the minerals having related structures based on stacking of HTB-type layers. The structural challenge for

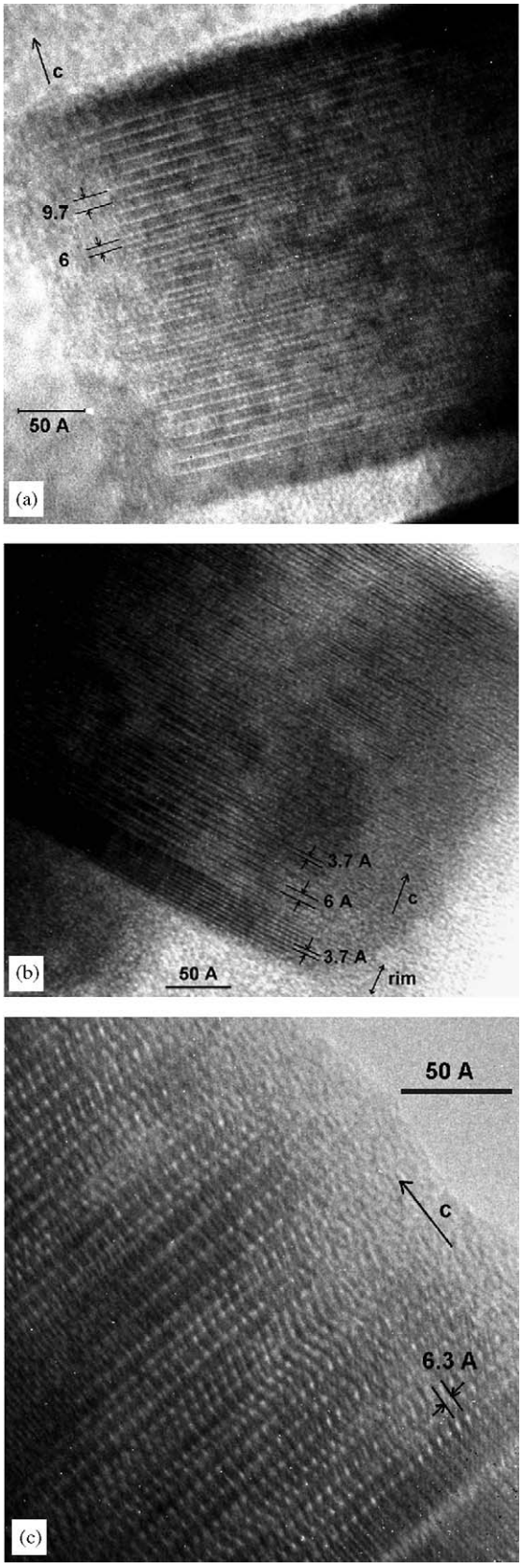

Fig. 5. Transmission electron microscope images of different crystals of pittongite, viewed parallel to the platelets. (a) and (b) Correspond to $[1\bar{1}0]$ zone axis images whereas (c) is a [110] zone axis image.

these minerals is to establish how the HTB layers are articulated.

4.1. Structural model for phyllotungstite

The nature of the HTB layer stacking is considered first for the case of phyllotungstite, because of its much smaller c-axis repeat. The presence of the 6_3 screw axis and the c glide plane both require the asymmetric unit to be no wider along c than $1/2c = 9.77$ Å. This distance corresponds to the fringe separation of ~9.7 Å observed in regions of the TEM images for pittongite shown in Fig. 5. The observation further supports the premise that pittongite and phyllotungstite have closely related structures. As seen in Fig. 5(b), the 9.7 Å (001) fringes are resolved under favourable imaging conditions into pairs of fringes with separations of 3.7 and 6 Å. The 3.7 Å component corresponds to the separation between pairs of HTB layers as shown in Fig. 1(c). The 6 Å separation, $\sim 1/3 \times 17.8$ Å, corresponds to the asymmetric unit repeat along c_{hex} for the rhombohedral pyrochlore structure. Such a representation of pyrochlore-type WO_3 is illustrated in Fig. 6, viewed along $[110]_{hex}$.

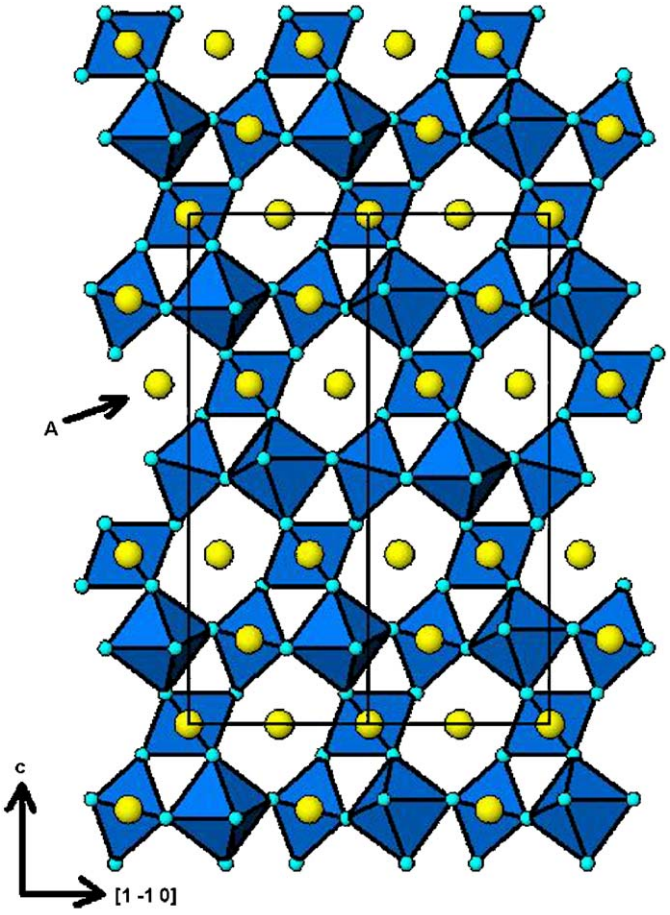

Fig. 6. Polyhedral representation of rhombohedral pyrochlore, viewed along [110] of the hexagonal cell. Large circles represent large-cation A sites.

Table 1
Atomic coordinates for phyllotungstite, described in a hexagonal unit cell, $a = 7.31(3)$ Å, $c = 19.55(1)$ Å, space group = $P6_3/mmc$

Atom	x	y	z
M1 (W, Al,)	0	0	0
M2 (W, Fe)	1/6	−1/6	0.159
A1 (H_2O, Ca, Pb)	0.5	0	0
A2 (H_2O, Ca, Pb)	2/3	1/3	0.159
O1	0.125	0.875	0.060
O2	0.459	0.541	0.130
O3	0.872	0.128	0.177
O4	0.210	0.790	$\frac{1}{4}$

A structural model for phyllotungstite that is consistent with the unit-cell symmetry and dimensions comprises pairs of HTB layers with a 3.7 Å separation, alternating with 6 Å thick $(111)_{py}$ slabs of pyrochlore structure. This represents a 1:1 intergrowth of the smallest repeating unit of both structures. It was straightforward to construct a model for the W atoms corresponding to this intergrowth in space group $P6_3/mmc$. Coordinates for the oxygen atoms were derived from the published single-crystal study on the phase $Pb_2Nb_2O_7$ [17]. This phase contains pyrochlore-type slabs of corner-connected NbO_6 octahedra that are stacked along the c-axis in a trigonal unit cell with $a = 7.472$ Å, $c = 28.35$ Å. The fractional coordinates were rescaled to the c-axis length for phyllotungstite. The connectivity of the model thus constructed was checked using ATOMS [18]. The calculated interatomic distances were sensible and within ranges for published tungsten oxide compounds, with M–O and O–O distances in the ranges 1.86–2.01 and 2.68–2.83 Å, respectively. By analogy with pyrochlore-type ferritungstite [2] the reported iron content (13.3 wt% Fe_2O_3) of phyllotungstite was incorporated at the W sites, while the reported minor amounts of Ca and Pb (1.8% CaO, 2.1% PbO) together with water molecules were distributed over the A-cation sites of the pyrochlore slabs.

The resulting atomic coordinates are given in Table 1 and a polyhedral representation of the octahedral framework in phyllotungstite is shown in projection along [110] in Fig. 7. The 3.7 Å separation between HTB layers and the 6 Å widths of the pyrochlore blocks are shown in Fig. 7. The model gives a satisfactory reproduction of the published powder diffraction data as seen from a comparison of the calculated and experimental patterns in Fig. 8. The peak intensities in the PXRD pattern are dominated by the contribution from the high-atomic number W atoms and thus no attempt was made to refine the positions and site occupancies of the lighter atoms, particularly in the absence of information on the quality of the published powder data [11].

4.2. Structural model for pittongite

Similar reasoning was used to develop a structural model for pittongite, based on intergrowth of HTB layers and

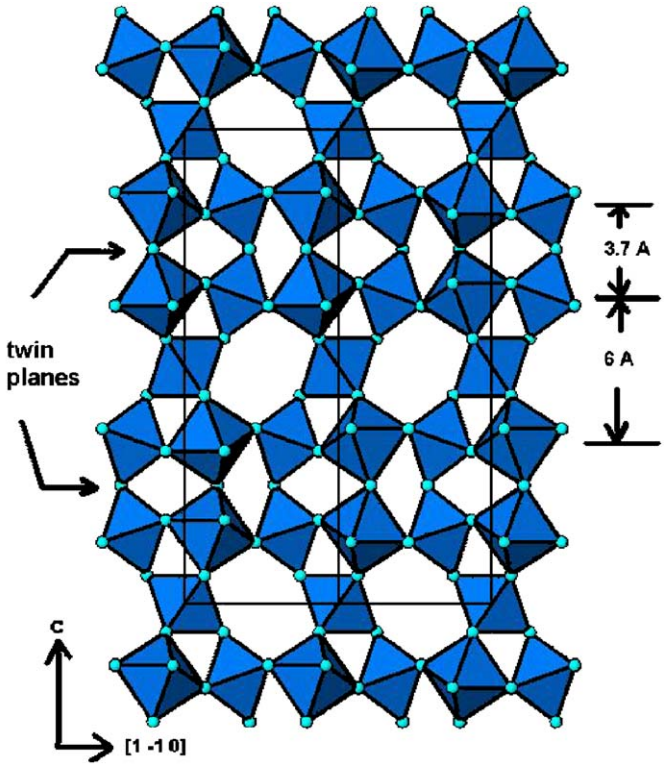

Fig. 7. Polyhedral representation of the octahedral $(W,Fe)_{14}(O,OH)_{42}$ framework for phyllotungstite, viewed along [110]. Arrows show location of mirror twin planes.

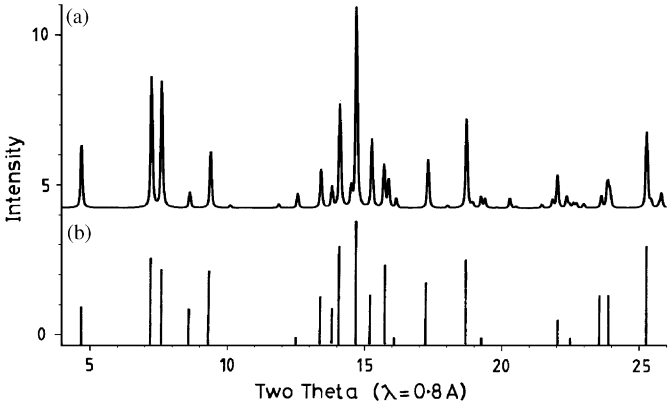

Fig. 8. (a) Calculated and (b) experimental (from Ref. [11]) PXRD patterns for phyllotungstite.

$(111)_{py}$ pyrochlore slabs. The TEM study on pittongite was helpful in providing information on the stacking sequence of the two structure types. As shown in Fig. 5, the (001) fringes in the TEM images have separations of either 9.7 or 6 Å. The average c-axis repeat of 50.5 Å obtained from indexing the SAED patterns corresponds to the combination of fringe spacings $(4 \times 9.7) + (2 \times 6)$, within the accuracy of measurement of the fringe separation. The different possible sequences of the two components corresponding to this combination are (9.7–9.7–6–9.7–9.7–6), (9.7–9–7–9.7–9.7–6–6) and (9.7–9.7–9.7–6–9.

7–6). Only the third sequence is consistent with the hexagonal symmetry; the other two sequences have rhombohedral symmetry.

After some experimentation with different space groups, it was found that a model having the third fringe-separation sequence (9.7–9.7–9.7–6–9.7–6) could be constructed using the hexagonal space group *P*-6*m*2, which is a subgroup of $P6_3/mmc$. As discussed in the previous section, the 9.7 Å fringes correspond to the sum of the separation between pairs of HTB layers (3.7 Å) and the basic repeat unit along c_{hex} of the rhombohedral pyrochlore structure (6 Å). The observed fringe sequence can thus be decomposed into HTB and pyrochlore elements according to the sequence (3.7–6–3.7–6–3.7–6–6–3.7–6–6). Following the procedure used for phyllotungstite, the atomic coordinates were established by appropriate rescaling and shifting along the *z*-axis of the published coordinates of the metal and oxygen atoms in the $(111)_{py}$ pyrochlore blocks of $Pb_2Nb_2O_7$ [17]. An ATOMS [18] check on the constructed model gave sensible M–O and O–O distances in the ranges 1.87–2.03 and 2.66–2.88 Å, respectively. By analogy with the iron tungsten oxide mineral ferritungsite, having a pyrochlore-type structure [2], the iron atoms were located with tungsten in the octahedral framework. The sodium atoms and water molecules were located at the *A*-cation positions in the pyrochlore slabs. The atomic coordinates are given in Table 2 and a polyhedral representation of the structure viewed along [110] is shown in Fig. 9. The sites occupied by Na and H_2O (the *A*-sites of the pyrochlore blocks) are shown by the circles in Fig. 9.

In fitting the structural model to the PXRD pattern using the Rietveld method, it was necessary to include a model for the impurity phase giving the broad peaks such as that marked with an arrow in Fig. 3. As discussed above, this phase was identified with the surface alteration phase observed in the TEM images. The spacings measured from

Table 2
Atomic coordinates for pittongite, in *P*-6*m*2, $a = 7.286(1)$ Å, $c = 50.49(1)$ Å

Atom	*x*	*y*	*z*
M1 (W, Fe, Al)	$\frac{1}{2}$	$\frac{1}{2}$	0.0359
M2 (W, Fe, Al)	2/3	1/3	0.0953
M3 (W, Fe, Al)	5/6	1/6	0.1547
M4 (W, Fe, Al)	5/6	1/6	0.2265
M5 (W, Fe, Al)	2/3	1/3	0.2859
M6 (W, Fe, Al)	$\frac{1}{2}$	$\frac{1}{2}$	0.3453
M7 (W, Fe, Al)	1/3	2/3	0.4047
M8 (W, Fe, Al)	1/6	5/6	0.4641
A1 (H_2O, Na, Ca)	0	0	0.036
A2 (H_2O, Na, Ca)	1/6	1/3	0.095
A3 (H_2O, Na, Ca)	1/3	2/3	0.155
A4 (H_2O, Na, Ca)	1/3	2/3	0.226
A5 (H_2O, Na, Ca)	1/6	1/3	0.286
A6 (H_2O, Na, Ca)	0	0	0.345
A7 (H_2O, Na, Ca)	1.3	1/6	0.405
A8 (H_2O, Na, Ca)	2/3	1/3	0.464
O1	0.2059	0.7941	0.0436
O2	0.5396	0.4604	0.0730
O3	0.7963	0.2037	0.1156
O4	0.1256	0.8744	0.1452
O5	0.5390	0.4610	0.1587
O6	0.8682	0.1318	0.1906
O7	0.5390	0.4610	0.2225
O8	0.1256	0.8744	0.2360
O9	0.7963	0.2037	0.2642
O10	0.5396	0.4604	0.3081
O11	0.2059	0.7941	0.3376
O12	0.7941	0.2059	0.3530
O13	0.4604	0.5396	0.3824
O14	0.2037	0.7963	0.4250
O15	0.8744	0.1256	0.4546
O16	0.4610	0.5390	0.4681
O17	0.1318	0.8682	$\frac{1}{2}$
O18	0.7941	0.2059	0.0282
O19	0.4604	0.5396	0

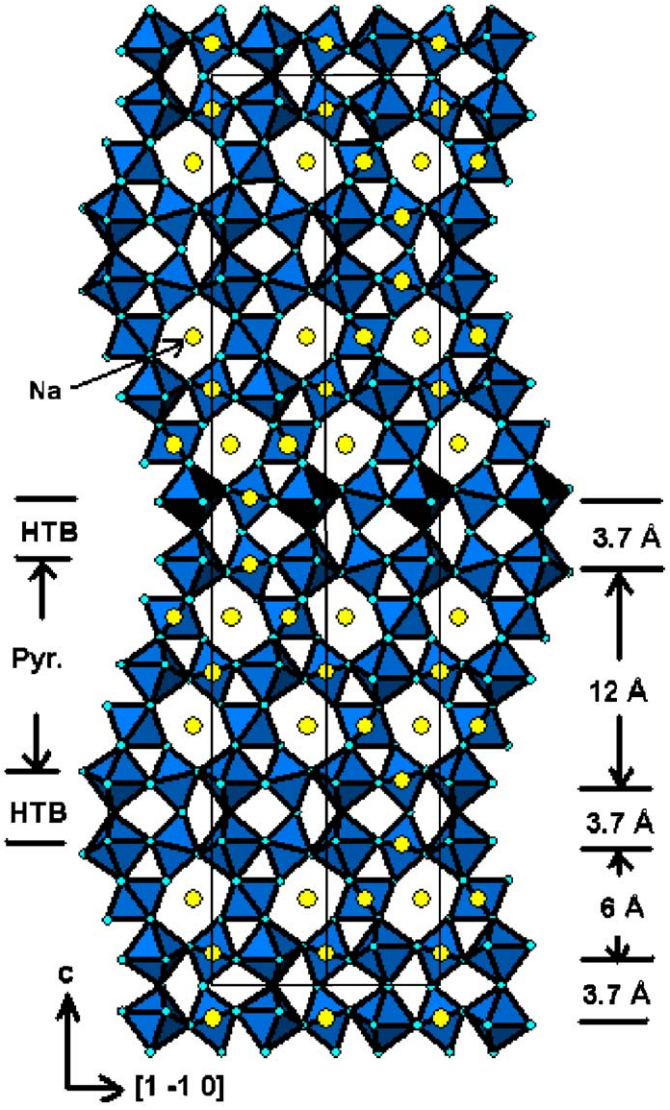

Fig. 9. Polyhedral representation of the locally ordered structure for pittongite, viewed along [110].

the TEM images for the surface phase, and its coherency with the core material, were consistent with it being a HTB-type structure. In the Rietveld calculation, it was assumed that the phase was hexagonal WO_3 and the reported [9] structural parameters for this phase were used in the Rietveld calculations. Indirect evidence for the broad peaks being due to a surface h-WO_3 phase is that the peak marked with an arrow in Fig. 3 indexes as (001), and its peak width corresponds to a crystallite size in the direction of the c-axis of 3 nm. This thickness matches with the directly measured thickness of the surface phase in TEM images such as shown in Fig. 5. The (00 ± 1) reflections due to the surface HTB phase are marked with an arrow in the SAED pattern for pittongite in Fig. 4(b).

In the Rietveld fitting to the synchrotron PXRD data, only the profile parameters were refined (background, scale factors for the two phases, cell parameters and peak widths). Refinement of structural parameters was not attempted, given the dominant contribution of W to the diffraction intensities as well as the peak fitting problems associated with the anisotropic particle shapes and the lack of long-range order in the c_{hex} direction for the intergrowth mineral. The fit parameters were $wR_p = 8.9$, $R_B = 6.4$ for the intergrowth phase and $R_B = 3.1\%$ for h-WO_3. The observed and calculated d spacings and relative intensities for the powder diffraction lines for pittongite are reported in Table 3.

Table 3
Indexed X-ray powder diffraction data for pittongite

I	D_{obs}	D_{calc}	Index
32	6.270	6.310	0 1 0
		6.262	0 1 1
52	5.956	6.122	0 1 2
		5.908	0 1 3
4	5.339	5.352	0 1 5
22	5.030	5.049	0 0 10
8	3.640	3.643	1 1 0
6	3.412	3.427	1 1 5
62	3.306	3.343	1 1 6
		3.308	0 1 13
100	3.153	3.156	0 0 16
		3.149	0 2 1
91	3.111	3.131	0 2 2
		3.101	0 2 3
21	3.006	3.011	0 2 5
30	2.951	2.954	1 1 10
		2.953	0 2 6
59	2.450	2.449	0 2 13
9	2.384	2.385	1 2 0
8	2.104	2.103	0 3 0
17	2.043	2.035	0 3 6
		2.033	0 2 19
42	1.945	1.946	1 2 15
		1.942	0 0 26
76	1.823	1.822	2 2 0
13	1.748	1.750	1 3 0
		1.750	2 2 24
23	1.716	1.714	1 1 26
		1.713	2 2 10
64	1.578	1.578	2 2 16
35	1.463	1.462	0 4 13
13	1.446	1.448	2 3 0
16	1.429	1.427	0 3 26
28	1.330	1.329	2 2 26
44	1.192	1.193	2 2 32

5. Discussion

The structures of pittongite and phyllotungstite can both be described in terms of intergrowths of $(111)_{py}$ pyrochlore blocks with pairs of HTB layers. In phyllotungstite the pyrochlore blocks are all of the same width = 6 Å, whereas pittongite contains pyrochlore blocks of two different widths, 6 and 12 Å. The TEM images for pittongite in Fig. 5 show that the intergrowth sequence is somewhat irregular and varies from one crystallite to another. The structure determined for pittongite, shown in Fig. 9, is a locally ordered variant that is consistent with the observed symmetry and average c-axis periodicity of 50.5 Å. Fig. 10 shows a comparison of this structural model with a selected region of the TEM image shown in Fig. 5(c). In the TEM image the defocus and sample thickness conditions are such that the regions of relatively low projected electron density appear as bright spots. A comparison of the image and structure in Fig. 10 shows a one-to-one match between the bright spots in the image and the sites occupied by the light atoms Na and H_2O, which occupy the centres of the hexagonal rings in the pyrochlore blocks.

A comparison of the structures for phyllotungstite and pittongite with that for pyrochlore, shown in the same projection in Fig. 6, shows that they may alternatively be described in terms of "chemical" twinning [19] of the pyrochlore structure on $(111)_{py}$. The oxygen atoms shared

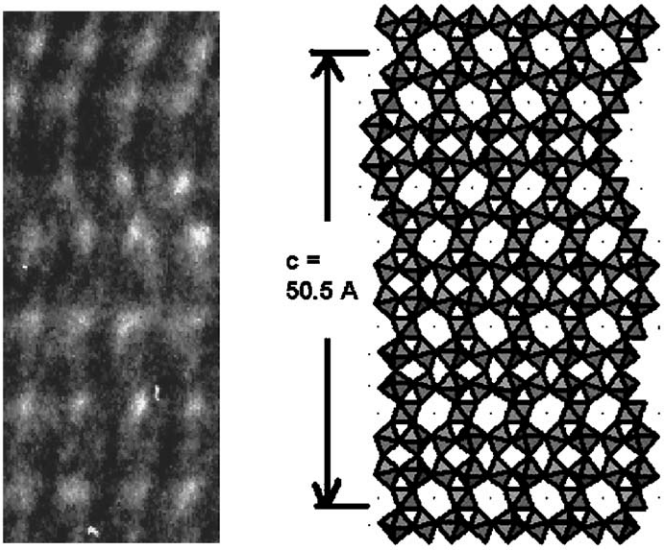

Fig. 10. Left-hand image is a [110] zone axis TEM image of pittongite. Right hand side is a [110] polyhedral projection of the structure model. There is a 1:1 match of the bright spots in the TEM image with the hexagonal channels in the intergrowth structure.

between each pair of HTB layers lie in the twin planes, which are simple mirror planes. These occur at $z = \frac{1}{4}$ and $\frac{3}{4}$ in phyllotungstite and at $z = 0$ and $\frac{1}{2}$ in pittongite. In the latter case there are also pseudo-mirror twin planes at $z = \pm 0.19$.

Unit-cell compositions can be calculated from combining the chemical analyses with the results from the structure analyses. For phyllotungstite the unit-cell octahedral framework composition is $M_{14}X_{42}$. If all available A sites are occupied the unit-cell formula is $A_{10}M_{14}X_{42}$. Scaling the number of W + Fe atoms in the published [11] formula to 14, and incorporating hydroxyl anions at X for charge balance gives the unit-cell composition for phyllotungstite as $[(H_2O)_{8.78}Ca_{0.94}Pb_{0.28}]_{\Sigma 10}[W_{9.14}Fe_{4.86}]_{\Sigma 14}[O_{29.86}OH_{12.14}]_{\Sigma 42} \cdot 1.6H_2O$. The calculated density based on this composition and the hexagonal unit cell is 5.40 g/cm^3. The formula differs markedly from that reported [11]. In the absence of a structural model, a formula was proposed [11] that was based on tetrahedral WO_4 groups, as in the primary tungstates such as ferberite and scheelite.

For pittongite the general unit-cell composition, based on occupation of all available A sites is $A_{28}M_{36}X_{108}$. Scaling the chemical analyses so that the number of atoms of Fe + W + Al = 36, gives the unit-cell composition for pittongite as $[(H_2O)_{16.0}Na_{7.8}K_{0.1}Ca_{0.6}]_{\Sigma 24.5}[W_{29.4}Fe_{5.8}Al_{0.8}]_{\Sigma 36}[O_{97.3}OH_{10.7}]_{\Sigma 108}$. With part of the analysed water assigned as hydroxyls for charge balance, the remaining water content plus the large cations Na, K and Ca sum to 24.5, giving incomplete occupancy of the 28 available A cation sites. The calculated density for pittongite is 5.71 g/cm^3; the higher density compared with that for phyllotungstite is due mainly to the higher W/Fe ratio. The calculated unit-cell composition and density values do not take into account a possibly different composition of the surface h-WO_3 coating. The coating is much too thin to obtain a separate microprobe analysis on it.

6. Conclusions

Crystal chemistry reasoning, aided with information from TEM images and PXRD data, has led to the development of structural models for pittongite, a new hydrated tungsten oxide mineral from southeastern Australia, and for the previously reported secondary tungsten mineral phyllotungstite [11]. Both minerals can be described in terms of chemical twinning of the pyrochlore structure on $(111)_{py}$ oxygen planes, giving hexagonal structures with $a_{hex} \sim 7.3$ Å and with c_{hex} a function of the width of the twinned pyrochlore blocks. In phyllotungstite, the $(111)_{py}$ blocks have the same thickness whereas pittongite contains twinned pyrochlore blocks of two thicknesses. At the twin planes, pairs of HTB layers are interconnected by corner sharing as in the HTB and h-WO_3 structures.

The structures can alternatively be described as unit-cell intergrowths of pyrochlore-type and HTB-type structures. In phyllotungstite, the intergrowth components represent the smallest possible repeating units of HTB and $(111)_{py}$ pyrochlore structures, with thicknesses of 3.7 and 6 Å, respectively, and they are intergrown on a 1:1 basis, (3.7-6-3.7-6). In pittongite the two different pyrochlore blocks have thicknesses of 6 and 2×6 Å. An ordered sequence of pyrochlore blocks in pittongite that is consistent with the observed symmetry and average c-axis periodicity is (3.7–6–3.7–6–3.7–6–6–3.7–6–6). It is thus a composite intergrowth of phyllotungstite and an intergrowth with 12 Å wide pyrochlore blocks. Pittongite is a relatively disordered alteration mineral and the local intergrowth sequence varies somewhat from one crystallite to another. Previously, it has been reported that low-temperature hydrothermal treatment of acidified tungstate solution leads to phases with either a defect pyrochlore structure or a HTB structure [16]. However, this appears to be the first reported instance of the characterization of minerals in which the two structure types are intergrown on the scale of the unit cell to form new intergrowth structures. Yagi and Roth [20] have reported on the intergrowth of HTB and pyrochlore blocks in synthetic mixed oxides in the system Rb_2O–Nb_2O_5. However in these phases the HTB/pyrochlore blocks are further intergrown with double HTB layers that are connected by edge sharing and corner sharing, so that they cannot be simply described as periodically twinned pyrochlore structures, as is the case for pittongite and phyllotungstite.

Acknowledgments

The synchrotron data collection was undertaken at the Australian National Beamline Facility with support from the Australian Synchrotron Research Program which is funded by the Major National Research Facilities Program. Alexander Priymak is thanked for assistance with the electron microprobe analyses.

References

[1] Th.G. Sahama, Mineral. Rec. 12 (1981) 81–87.
[2] T.S. Ercit, G.W. Robinson, Can. Mineral. 32 (1994) 567–574.
[3] J.W. Anthony, R.A. Bideaux, K.W. Bladh, M.C. Nichols, Handbook of Mineralogy, Halides, Hydroxides, Oxides, vol. III, Mineral Data Publishing, Tucson, AZ, 1997.
[4] P.A. Williams, P. Leverett, J.L. Sharpe, D.M. Colchester, Can. Mineral. 43 (2005) 1061–1064.
[5] J.T. Szymanski, A.C. Roberts, Can. Mineral. 22 (1984) 681–688.
[6] Th.G. Sahama, M. Lehtinen, Bull. Geol. Soc. Finland 43 (1971) 89–91.
[7] B. Gerand, G. Nowogrocki, M. Figlarz, J. Solid State Chem. 38 (1981) 312–320.
[8] J.R. Gunter, M. Amberg, H. Schmalle, Mater. Res. Bull. 24 (1989) 289–292.
[9] B. Gerand, G. Nowogrocki, J. Guenot, M. Figlarz, J. Solid State Chem. 29 (1979) 429–434.
[10] L. Seguin, B. Gerand, G. Chevrier, M. Toubou, Mater. Sci. Forum 228–231 (1996) 695–700.
[11] K. Walenta, N. J. Miner. Mh. 12 (1984) 529–535.
[12] W.D. Birch, S.J. Mills, I.E. Grey, C. Bougerol, S. Ansermet, A. Pring, Can. Mineral. (2006) (in press).

[13] R.J. Hill, C.J. Howard, A computer program for Rietveld analysis of fixed wavelength X-ray and neutron powder diffraction patterns, in: AAEC Report Number M112, Australian Atomic Energy Commission, Sydney, Australia, 1986.
[14] J. Laugier, B. Bochu, LMGP — program for the interpretation of X-ray experiments, INPG/Laboratoire des Materiaux et du Genie Physique, St. Martin d'Heres, France, 2000.
[15] I.E. Grey, A.F. Reid, J. Solid State Chem. 4 (1972) 186–194.
[16] K.P. Reis, A. Ramanan, M.S. Whittingham, J. Solid State Chem. 96 (1992) 31–47.
[17] H. Bernotat-Wulf, W. Hoffman, Z. Kristallogr. 158 (1982) 101–117.
[18] E. Dowty, ATOMS for Windows, vsn. 6.1. Shape Software, Kingsport, USA, 2004.
[19] S. Andersson, B.G. Hyde, J. Solid State Chem. 9 (1974) 92–101.
[20] K. Yagi, R.S. Roth, Acta Crystallogr. A 34 (1978) 765–773.